

# MIMO Beam Map Reconstruction via Toeplitz-Structured Matrix-Vector Tensor Decomposition

Hao Sun, Junting Chen, *Member, IEEE*, and Xianghao Yu, *Senior Member, IEEE*

**Abstract**—As wireless networks progress toward sixth-generation (6G), understanding the spatial distribution of directional beam coverage becomes increasingly important for beam management and link optimization. Multiple-input multiple-output (MIMO) beam map provides such spatial awareness, yet accurate construction under sparse measurements remains difficult due to incomplete spatial coverage and strong angular variations. This paper presents a tensor decomposition approach for reconstructing MIMO beam map from limited measurements. By transforming measurements from a Cartesian coordinate system into a polar coordinate system, we uncover a matrix-vector outer-product structure associated with different propagation conditions. Specifically, we mathematically demonstrate that the matrix factor, representing beam-space gain, exhibits an intrinsic Toeplitz structure due to the shift-invariant nature of array responses, and the vector factor captures distance-dependent attenuation. Leveraging these structural priors, we formulate a regularized tensor decomposition problem to jointly reconstruct line-of-sight (LOS), reflection, and obstruction propagation conditions. Simulation results confirm that the proposed method significantly enhances data efficiency, achieving a normalized mean square error (NMSE) reduction of over 20% compared to state-of-the-art baselines, even under sparse sampling regimes.

**Index Terms**—Matrix-vector, MIMO beam map, polar coordinate system, sparse measurements, tensor decomposition, Toeplitz.

## I. INTRODUCTION

Massive multiple-input multiple-output (MIMO) has become a key enabler for fifth-generation (5G) and is expected to remain central in future sixth-generation (6G) networks, owing to its ability to provide high spatial multiplexing gains, strong beamforming gains, and flexible interference mitigation [1]–[3]. However, fully harvesting these benefits requires high-dimensional channel state information (CSI), which leads to substantial channel training and feedback overhead. To alleviate this burden, the MIMO beam map has emerged as a structured representation that describes the spatial distribution of

Hao Sun was with the School of Science and Engineering (SSE), Shenzhen Future Network of Intelligence Institute (FNii-Shenzhen), and Guangdong Provincial Key Laboratory of Future Networks of Intelligence, The Chinese University of Hong Kong, Shenzhen, Guangdong 518172, China. He is now with the Department of Electrical Engineering, City University of Hong Kong, Hong Kong (e-mail: hao.sun@cityu.edu.hk).

Junting Chen is with the School of Science and Engineering (SSE), Shenzhen Future Network of Intelligence Institute (FNii-Shenzhen), and Guangdong Provincial Key Laboratory of Future Networks of Intelligence, The Chinese University of Hong Kong, Shenzhen, Guangdong 518172, China (e-mail: juntingc@cuhk.edu.cn).

Xianghao Yu is with the Department of Electrical Engineering, City University of Hong Kong, Hong Kong (e-mail: alex.yu@cityu.edu.hk).

directional beams, signal strength, and link quality across the coverage area [4], [5]. By enabling interference management, adaptive beamforming, and energy-efficient power allocation without exhaustive channel training [6], [7], MIMO beam map provides a powerful tool for planning and optimizing dense urban and complex indoor deployments [8]–[10].

Nevertheless, how to efficiently construct accurate MIMO beam map from limited measurements remains largely unexplored. A first challenge arises from the incomplete spatial coverage due to sparse measurements. When observations are limited, it is hard to fully capture beam propagation patterns or signal interactions, resulting in missing regions and underrepresented areas in the map. Second, MIMO beam map typically exhibits stronger spatial variations, as the received signal strength (RSS) is influenced not only by the propagation environment but also by the beamforming pattern. Consequently, conventional interpolation- or tensor-based methods generally require a larger number of measurements to achieve satisfactory accuracy.

MIMO beam map can be viewed as a particular type of radio map [11]. Classical interpolation methods, such as Kriging [12], [13], local polynomial regression [14], and kernel-based schemes [15], estimate unobserved locations by exploiting spatial smoothness or neighborhood information. Kriging typically models spatial correlation functions explicitly, which may incur substantial computational overhead in large-scale scenarios and may require prior knowledge of the underlying spatial structure. Local polynomial regression and kernel-based approaches rely on locality and smoothness assumptions, which may become less effective when dealing with high-dimensional feature spaces or irregularly distributed measurements. Matrix-based methods leverage the observation that radio maps, when arranged in matrix form, often exhibit low-rank characteristics. This property enables techniques such as Bayesian learning [16], [17], dictionary learning [18] and matrix completion [19] to infer missing measurements or extrapolate beam-related information in unobserved regions. Tensor-based methods [7], [20], [21] further exploit multi-dimensional structures inherent in radio maps by modeling correlations across multiple domains, such as space, frequency, or beam indices, using low-rank tensor decomposition. However, these methods may not fully utilize the underlying latent structure in MIMO beam map, which arises from distinct beam patterns associated with various angles.

Deep learning-based approaches including variational autoencoder (VAE) [22], generative adversarial network (GAN)

[23]–[25], and diffusion-based methods [26], [27], treat the radio map as one or more layers of 2D images, using neural networks to recognize common patterns based on extensive training data. These approaches require large amounts of training data, which may not always be available.

To exploit the underlying structure embedded in beam patterns across different beam indices, this paper first transforms the sparse Cartesian measurements into a polar coordinate system parameterized by the beam angle at the base station (BS), the spatial angle of the user equipment (UE), and the propagation distance. These measurements are then aggregated into a three-dimensional (3D) tensor, where each entry corresponds to the RSS value within a specific polar bin defined by the angle and distance parameters. Under different propagation conditions (e.g., line-of-sight (LOS), reflection, and obstruction), the resulting tensor exhibits a matrix-vector outer-product structure. The matrix factor, referred to as the beam-space gain, captures the interaction between the beam-forming pattern and the spatial angles of the UE, whereas the vector factor models distance-dependent power attenuation. Furthermore, the beam-space gain matrix is shown to exhibit an inherent Toeplitz structure, reflecting the shift-invariant angular correlation induced by angular sampling and beam index ordering.

Building on this structural insight, we develop a Toeplitz-structured matrix-vector tensor decomposition framework to reconstruct the MIMO beam map in the presence of multiple propagation conditions. In the general case where LOS, reflection, and obstruction components coexist, the beam-space tensor is modeled as a sum of a few matrix-vector terms, each corresponding to one propagation condition. The resulting optimization problem is tackled via an alternating minimization procedure. Specifically, the matrix factors are updated by proximal-gradient iterations under the Toeplitz regularization, whereas the vector factors are obtained from a constrained quadratic program.

The contributions of this paper are summarized as follows:

- We propose a tensor representation based on polar coordinate transformation for MIMO beam map construction. The tensor model takes the form of matrix-vector outer-products, where the matrix component is shown to exhibit a Toeplitz structure that enables efficient construction under sparse samples.
- We develop a generalized Toeplitz-structured tensor decomposition formulation to handle complex scenarios with strong reflections and obstructions. Specifically, we incorporate a soft Toeplitz regularization for the beam-space matrices, coupled with monotonicity constraints on the distance-domain attenuation vectors to ensure physical consistency.
- We design a structure-aware alternating minimization for the proposed matrix-vector tensor decomposition model. For general propagation scenarios, the algorithm alternately updates the beam-space gain matrix and the distance-domain attenuation vectors via a Toeplitz-like regularization. For a special case, where only a pure LOS region exists, we further exploit the symmetric Toeplitz structure and impose it as a hard constraint, which allows

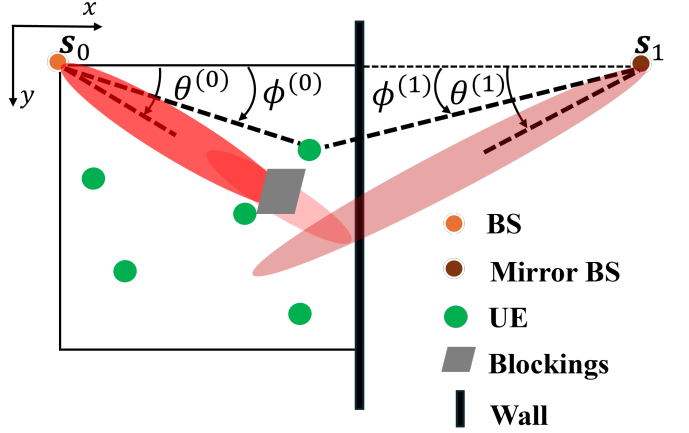


Figure 1. Complex scenario showing a direct path from the BS, a reflected path via the mirror BS, and an obstructed path affected by physical blockings.

each beam-space gain matrix to be parameterized by a single Toeplitz row and estimated via a closed-form least-squares update, reducing the degrees of freedom and computational complexity.

- Extensive simulations across different sampling ratios and propagation environments demonstrate that the proposed Toeplitz-structured tensor decomposition method obtains more than 20% improvement in reconstruction NMSE compared with KNN, TPS, and conventional BTD-based baselines.

The rest of the paper is organized as follows. Section II introduces the propagation, beam, and measurement models. Section III develops a structured tensor representation of the MIMO beam map by transforming Cartesian measurements into the polar domain and revealing the underlying Toeplitz matrix-vector structure. Section IV formulates the Toeplitz-regularized matrix-vector tensor decomposition problem and presents an alternating minimization algorithm for its solution. Section V derives simplified decomposition models for a pure LOS region. Numerical results are presented in Section VI and conclusion is given in Section VII.

*Notation:* Vectors are written as bold italic letters  $\mathbf{x}$ , matrices as bold capital italic letters  $\mathbf{X}$ , and tensors as bold calligraphic letters  $\mathcal{X}$ . For a matrix  $\mathbf{X}$ ,  $[\mathbf{X}]_{ij}$  denotes the entry in the  $i$ th row and  $j$ th column of  $\mathbf{X}$ . For a tensor  $\mathcal{X}$ ,  $[\mathcal{X}]_{i,j,k}$  denotes the entry under the index  $(i, j, k)$ . The symbol ‘ $\circ$ ’ represents the outer product, ‘ $*$ ’ represents the element-wise product,  $\|\cdot\|_2$  represents the  $l_2$  norm, and  $\|\cdot\|_F$  represents the Frobenius norm. The operator  $\text{vec}(\cdot)$  stacks the columns of a matrix (or the entries of a tensor slice) into a column vector, and  $\text{diag}(\mathbf{x})$  denotes a diagonal matrix with the entries of  $\mathbf{x}$  on its main diagonal. The transpose is denoted by  $(\cdot)^T$ .  $\mathbb{E}\{\cdot\}$  denotes statistical expectation.  $\mathcal{O}(x)$  means  $|\mathcal{O}(x)|/x \leq C$ , for all  $x > x_0$  with  $C$  and  $x_0$  are positive real numbers.

## II. SYSTEM MODEL

### A. Propagation and Beam Model

Consider a downlink channel from the BS to user equipments (UEs) in an indoor environment. The BS, located at

the origin  $s_0 = (0, 0)$ , is equipped with a uniform linear antenna array (ULA) of  $N_t$  elements. The array elements are aligned along the  $y$ -axis, with their pointing direction toward the positive  $x$ -axis. The indoor region  $\mathcal{D}$  of interest is located in the first quadrant of the coordinate system as shown in Fig. 1.

Consider the radio propagation from  $s_0$  to any position in  $\mathcal{D}$ . Only a single reflection from the right wall in Fig. 1 is taken into account, since higher-order reflections suffer severe attenuation due to multiple propagation losses and thus contribute negligibly compared with the direct and single-reflection paths [28]. Thus, the right wall, which directly faces the BS, is the dominant reflector. According to the law of specular reflection, we introduce a mirror position  $s_1$ , defined such that the right wall is the perpendicular bisector of the line segment between  $s_0$  and  $s_1$ . In this way, the reflected path via the right wall is geometrically equivalent to a mirror direct path from the mirror BS at  $s_1$ .

The BS is configured with a set of  $I$  beams for environment sensing, where each beam has a single mainlobe pointing at a specific direction  $\theta_i$ ,  $i = 1, 2, \dots, I$ , and the sidelobes have significantly lower energy than that of the mainlobe. A typical example of constructing such beams under ULA is to use the set of discrete time Fourier transform (DFT) vectors for beamforming [2], [29]. As the BS is placed at the corner of  $\mathcal{D}$ , it suffices to only consider the beam directions  $\theta_i \in (0, \pi/2)$  for the sensing purpose.

Denote the array response vector  $\mathbf{e}(\theta) \in \mathbb{C}^{N_t}$  of the ULA at BS as

$$\mathbf{e}(\theta) = [1, \exp(-j\pi \sin \theta), \dots, \exp(-j\pi(N_t - 1) \sin \theta)]^T$$

where  $j = \sqrt{-1}$ . The channel vector  $\mathbf{h}$  for a position  $\mathbf{z} \in \mathcal{D}$  is modeled as

$$\mathbf{h} = \alpha_0 \mathbf{e}(\phi_0(\mathbf{z})) e^{-j2\pi f_c \tau_0} + \alpha_1 \mathbf{e}(\phi_1(\mathbf{z})) e^{-j2\pi f_c \tau_1} + \mathbf{h}^e \quad (1)$$

where  $\alpha_0$  and  $\tau_0$  denote, respectively, the complex gain and the delay of the direct path, which can possibly be significantly attenuated due to blockage. The function  $\phi_0(\mathbf{z})$  captures the angle from the BS at  $s_0$  to the position  $\mathbf{z}$ . Likewise,  $\alpha_1$  and  $\tau_1$  denote the complex gain and delay of the possible reflected path from the right wall. Note that, such a path can also be blocked or may not exist, leading to  $\alpha_1 \approx 0$ . The function  $\phi_1(\mathbf{z})$  captures the angle from the mirror BS to the position  $\mathbf{z}$ , representing the angle of the reflected path leaving. Finally, the term  $\mathbf{h}^e$  captures all the residual paths.

It is possible that the reflecting environment is more complicated and there are a few more mirror BSs. The construction of the reflection due to additional mirror BSs is similar to the second term in (1).

## B. Measurement Model

The direct and reflected paths can be separated by exploiting the inherent characteristics of received signals [28], [30]. Based on this, we establish the measurement model. For the  $i$ th beam, the RSS associated with the direct path at location  $\mathbf{z}_m$  is modeled as

$$\gamma_i^{(0)}(\mathbf{z}_m) = \mathbb{E} \left\{ \left| \alpha_0 \mathbf{w}_i^H \mathbf{e}(\phi_0(\mathbf{z}_m)) e^{-j2\pi f_c \tau_0} \right|^2 \right\} + n^{(0)} \quad (2)$$

where  $\mathbb{E}\{\cdot\}$  denotes the expectation over the randomness induced by small-scale fading contained in  $\alpha_0$ ,  $\mathbf{w}_i \triangleq \mathbf{e}(\theta_i)$  is the beamforming vector, and  $n^{(0)}$  captures the residual energy contributed by scattered paths whose delays are close to that of the direct path and thus cannot be fully resolved. We assume that  $n^{(0)}$  follows a Gaussian distribution, i.e.,  $n^{(0)} \sim \mathcal{N}(0, \sigma_0^2)$ .

Similarly, the RSS corresponding to the reflected path is modeled as

$$\gamma_i^{(1)}(\mathbf{z}_m) = \mathbb{E} \left\{ \left| \alpha_1 \mathbf{w}_i^H \mathbf{e}(\phi_1(\mathbf{z}_m)) e^{-j2\pi f_c \tau_1} \right|^2 \right\} + n^{(1)} \quad (3)$$

where  $n^{(1)}$  accounts for the energy of scattered paths that exhibit similar delays to the reflected path  $\alpha_1$  and thus cannot be distinguished. We also assume that  $n^{(1)} \sim \mathcal{N}(0, \sigma_1^2)$ .

In the above formulation, it is assumed that the direct path  $\alpha_0$  and the reflected path  $\alpha_1$  can be extracted from the channel vector  $\mathbf{h}$  with some uncertainty, represented by  $n^{(0)}$  and  $n^{(1)}$ , respectively. The accuracy of this extraction depends on the resolution capability of the power-angular-delay profile, which in turn is determined by the system bandwidth and antenna array structure.

Under this measurement model, the  $i$ th beam yields two types of observations at location  $\mathbf{z}_m$ , namely  $\gamma_i^{(0)}(\mathbf{z}_m)$  and  $\gamma_i^{(1)}(\mathbf{z}_m)$ , corresponding to the direct and reflected paths, respectively. Collecting all such observations forms two sparse measurement sets

$$\{(\theta_i, \mathbf{z}_m, \gamma_i^{(0)}(\mathbf{z}_m))\} \quad \text{and} \quad \{(\theta_i, \mathbf{z}_m, \gamma_i^{(1)}(\mathbf{z}_m))\}.$$

Our goal is to reconstruct the complete MIMO beam map from these sparse measurements.

## III. TOEPLITZ-STRUCTURED TENSOR MODEL VIA COORDINATE TRANSFORMATION

In this section, we show that by transforming the measurement set  $\{\theta_i, \mathbf{z}_m, \gamma_i^{(l)}(\mathbf{z}_m)\}$ , originally defined in the Cartesian coordinate system  $(x, y)$ , into the polar coordinate system  $(\phi, d)$ , the resulting tensor exhibits a matrix-vector structure, where under certain conditions, the matrix component becomes *Toeplitz*.

### A. Coordinate Transformation

We focus on the LOS scenario for illustrative purposes, as the reflected-path case can be handled in a similar way with the assistance from the mirror BS  $s_1$ . For notational simplicity, we omit the superscript ' $(l)$ ' in this subsection.

#### 1) Transformation from Cartesian to Polar Coordinates:

Recall that the BS is located at  $s_0 = (x_0, y_0)$ . For each measured UE position  $\mathbf{z}_m = (x_m, y_m)$ , its polar coordinates relative to  $s_0$  are defined as

$$d_m = \|\mathbf{z}_m - s_0\|_2, \quad \phi_m = \arctan \frac{y_m - y_0}{x_m - x_0} \quad (4)$$

where  $\arctan$  returns the polar angle of the point  $(x_m, y_m)$  with respect to (w.r.t.) the positive  $x$ -axis.

To construct the measurement tensor, we discretize the angular and radial domains into uniform grids

$$\{\phi_1, \dots, \phi_J\}, \quad \phi_j = (j - 1)\Delta_\phi$$

$$\{d_1, \dots, d_K\}, \quad d_k = (k-1)\Delta_d$$

where  $\Delta_\phi$  and  $\Delta_d$  denote the discretization steps in the angular and radial domains. Each measurement  $(\phi_m, d_m)$  is assigned to its nearest angular and radial bins  $(\phi_j, d_k)$  via

$$j = 1 + \left\lfloor \frac{\phi_m}{\Delta_\phi} \right\rfloor, \quad k = 1 + \left\lfloor \frac{d_m}{\Delta_d} \right\rfloor, \quad (5)$$

where  $\lfloor \cdot \rfloor$  denotes rounding to the nearest integer.

Denote the measurement  $\gamma_i(z_m)$  as  $\gamma_{m,i}$ . We then construct a structured tensor  $\mathcal{X} \in \mathbb{R}^{I \times J \times K}$  where the entry  $[\mathcal{X}]_{i,j,k}$  aggregates all measurements taken by beam  $\theta_i$  from the polar bin  $(\phi_j, d_k)$ :

$$[\mathcal{X}]_{i,j,k} = \begin{cases} \frac{1}{|\mathcal{S}_{j,k}|} \sum_{m \in \mathcal{S}_{j,k}} \gamma_{m,i}, & \text{if } \mathcal{S}_{j,k} \neq \emptyset \\ \text{unobserved,} & \text{otherwise} \end{cases} \quad (6)$$

where  $\mathcal{S}_{j,k}$  denotes the index set of the measurements whose angular and radial coordinates are in the bin  $(\phi_j, d_k)$ .

2) *Toeplitz Structure*: To understand the intrinsic structure of the tensor  $\mathcal{X}$ , we analyze the measurement model for the direct path established in (2). The first term in (2) represents the dominant signal component that we aim to model. For a location  $z_m$  with polar coordinates  $(\phi_j, d_k)$ , the RSS in (2) satisfies

$$\mathbb{E}\{\gamma_{m,i}\} = \mathbb{E}\{|\alpha_0|^2\} \cdot |\mathbf{e}^H(\theta_i)\mathbf{e}(\phi_j)|^2. \quad (7)$$

Then, (2) can be written as a product of a distance-dependent power attenuation term  $P(d_k)$  and a beamforming gain term  $\mathbf{e}^H(\theta_i)\mathbf{e}(\phi_j)$

$$\gamma_{m,i} = P(d_k) \cdot |\mathbf{e}^H(\theta_i)\mathbf{e}(\phi_j)|^2 + \epsilon \quad (8)$$

where  $P(d_k)$  approximates  $\mathbb{E}\{|\alpha_0|^2\}$  which decays with distance  $d_k$  and  $\epsilon \sim \mathcal{N}(0, \delta^2)$  captures the random noise that is not captured by the first term.

Based on the structure of (8), we define a distance-domain attenuation vector  $\rho \in \mathbb{R}^K$ , whose entries are given by  $\rho_k = P(d_k)$ . We further define a beam-space gain matrix  $\mathbf{G} \in \mathbb{R}^{I \times J}$ , which exclusively captures the interaction between the beamforming angles  $\theta_i$  and the spatial angles  $\phi_j$ . Its  $(i,j)$ -th entry is given by

$$\begin{aligned} [\mathbf{G}]_{i,j} &= |\mathbf{e}^H(\theta_i)\mathbf{e}(\phi_j)|^2 \\ &= \left| \sum_{n=0}^{N_t-1} \exp(j\pi n(\sin(\theta_i) - \sin(\phi_j))) \right|^2. \end{aligned} \quad (9)$$

Consequently, from (8)–(9), the measurements  $\gamma_{m,i}$  form a tensor  $\mathcal{X}$  that can be represented by a rank-1 matrix-vector outer product model

$$\mathcal{X} = \mathbf{G} \circ \rho + \mathcal{E}, \quad (10)$$

where  $\mathcal{E}$  captures the residual energy which is modeled as noise.

A crucial property of the beam-space gain matrix  $\mathbf{G}$  is that, under specific conditions, it becomes highly structured, i.e., Toeplitz and symmetric.

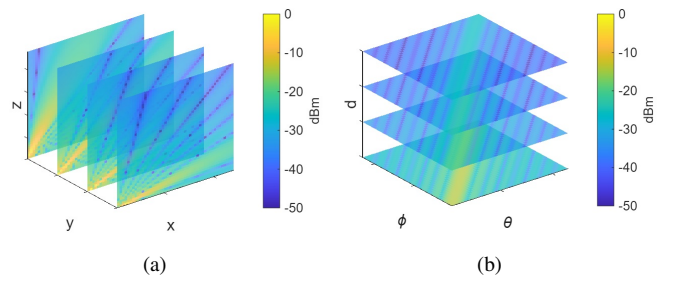


Figure 2. (a) The MIMO beam map under the Cartesian coordinate system. (b) The transformed MIMO beam map under the polar coordinate system, revealing Toeplitz and symmetric structures that can be exploited for structured reconstruction.

**Lemma 1** (Toeplitz and Symmetric Structure). *If the angles  $\theta_i$  and  $\phi_j$  are chosen such that their sines form uniform grids, i.e.,  $\sin(\theta_i) = i/I$  and  $\sin(\phi_j) = j/J$ , and  $I = J$ , then the matrix  $\mathbf{G}$  exhibits a Toeplitz and symmetric structure.*

*Proof.* See Appendix A.  $\square$

This structural property is of particular importance because it implies that the entire beam-space gain matrix  $\mathbf{G}$  only has a small degrees-of-freedom, thereby facilitating efficient tensor reconstruction from sparse measurements.

Fig. 2(a) shows the MIMO beam map  $\mathcal{X}$  represented in the Cartesian coordinate system, where the beam pattern across different directions can be directly visualized. However, in this form, the map does not explicitly exhibit exploitable structural properties. By contrast, Fig. 2(b) presents the direct beam component of  $\mathcal{X}$  in the polar coordinate system, in which clear Toeplitz and symmetry structures emerge. These structural characteristics are critical for enabling reliable reconstruction of the MIMO beam map from sparse measurements and are not readily observable in the Cartesian representation.

### B. Tensor Model under the Presence of Reflection and Obstruction

With the presence of reflection and obstruction, we propose a rank- $R$  superposition tensor model to capture the dominant effect of the propagation as

$$\mathcal{X} = \sum_{r=1}^R \mathbf{G}_r \circ \rho_r + \mathcal{E} \quad (11)$$

where each matrix  $\mathbf{G}_r \in \mathbb{R}^{I \times J}$  represents the beam-space gain pattern associated with the  $r$ -th propagation condition, and  $\rho_r \in \mathbb{R}^K$  models its corresponding distance-dependent attenuation. The rank  $R$  reflects the number of propagation conditions in the environment, typically characterized by the coexistence of LOS, reflection, and obstruction.

The general model (11) can be adapted to capture various propagation scenarios, as outlined in the following subsections.

1) *Pure LOS Region*: In the pure LOS region where there is no strong reflection, as illustrated in Fig. 3(a), the tensor  $\mathcal{X}$  can be represented by a simple matrix-vector tensor decomposition as in (10), where the rank in (11) reduces to  $R = 1$ .

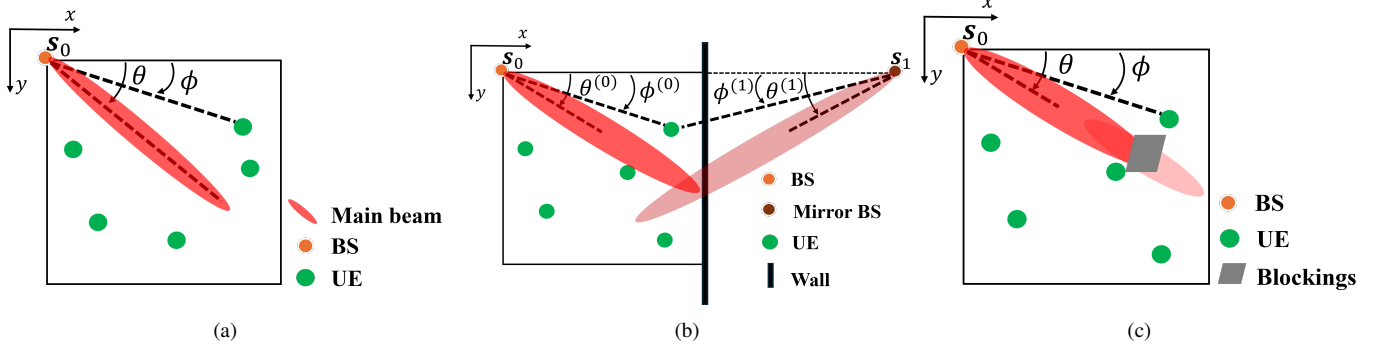


Figure 3. Three common beam propagation scenarios: (a) Pure LOS Region. (b) Coexistence of LOS and Reflection. (c) Coexistence of LOS and Obstruction.

2) *Coexistence of LOS and Reflection*: For a region where LOS and reflection coexist, as illustrated in Fig. 3(b), similar to (7)–(8), the measurements corresponding to each propagation condition can be written as

$$\gamma_{m,i}^{(l)} = P(d_k^{(l)}) \cdot |e^H(\theta_i)e(\phi_j^{(l)})|^2 + \epsilon$$

where  $l = 0$  denotes the LOS condition and  $l = 1$  denotes the reflection condition. For each propagation condition, the measurement tensor  $\mathcal{X}$  can be represented by a simple matrix-vector tensor decomposition

$$\mathcal{X}^{(l)} = \mathbf{G}^{(l)} \circ \boldsymbol{\rho}^{(l)} + \mathcal{E}, \quad l = 0, 1.$$

Since the reflection originates from a mirror BS  $s_1$ , which has an identical beam pattern as the BS  $s_0$ , under the same scope of  $\phi_j^{(0)}$  and  $\phi_j^{(1)}$ , we have  $\mathbf{G}^{(0)} = \mathbf{G}^{(1)} \triangleq \mathbf{G}$ . By concatenating the separated measurements along the distance dimension, an augmented tensor can be constructed as

$$\mathcal{X} = \text{cat}(\mathcal{X}^{(0)}, \mathcal{X}^{(1)}) + \mathcal{E} = \mathbf{G} \circ \boldsymbol{\rho} + \mathcal{E} \quad (12)$$

where  $\boldsymbol{\rho} = [\boldsymbol{\rho}^{(0)}; \boldsymbol{\rho}^{(1)}] \in \mathbb{R}^{2K}$ . This construction preserves the rank-1 structure of the tensor.

3) *Coexistence of LOS and Obstruction*: In the case where the direct path is partially obstructed, as illustrated in Fig. 3(c), two distinct conditions exist: a LOS region before the obstruction and an NLOS region after it.

Consequently, the formulation in (8) is modified as

$$\gamma_{m,i} = P_0(d_k, \phi_j) \cdot |e^H(\theta_i)e(\phi_j)|^2 + \epsilon \quad (13)$$

where the power attenuation term  $P_0$  now depends jointly on both  $d_k$  and  $\phi_j$ . For a fixed  $d_k$ , different  $\phi_j$  may correspond to either LOS or NLOS regions, resulting in a lower received power  $\gamma_{m,i}$  when blockage exists.

To explicitly capture the angular dependence, we further express (13) as

$$\gamma_{m,i} = P(d_k) \cdot \alpha(\phi) |e^H(\theta_i)e(\phi_j)|^2 + \epsilon \quad (14)$$

where  $\alpha(\phi)$  is a directional attenuation factor that varies with  $\phi$ . Accordingly, for distance  $d_k$  where both LOS and NLOS regions coexist, we approximate the corresponding measurements  $\gamma_{m,i}$  using  $\mathbf{G}_2 \circ \boldsymbol{\rho}_2$ , while the purely LOS region is represented by  $\mathbf{G}_1 \circ \boldsymbol{\rho}_1$ . This leads to a rank- $R = 2$  model in

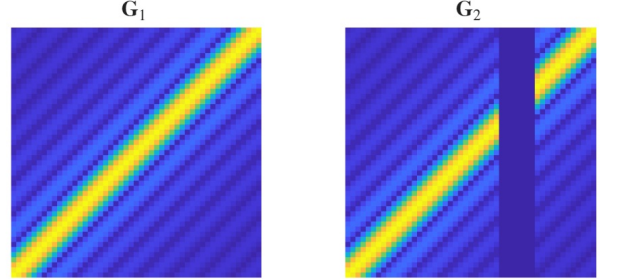


Figure 4. Visible plots of  $\mathbf{G}_1$  and  $\mathbf{G}_2$ .  $\mathbf{G}_1$  exhibits a Toeplitz structure corresponding to the LOS region, while  $\mathbf{G}_2$  displays a quasi-Toeplitz pattern with a dark region indicating signal obstruction.

which the overall tensor is expressed as a sum of two rank-one components

$$\mathcal{X} = \mathbf{G}_1 \circ \boldsymbol{\rho}_1 + \mathbf{G}_2 \circ \boldsymbol{\rho}_2 + \mathcal{E}. \quad (15)$$

A visual description of  $\mathbf{G}_1$  and  $\mathbf{G}_2$  is shown in Fig. 4. The matrix  $\mathbf{G}_1$  exhibits a clear Toeplitz structure, whereas  $\mathbf{G}_2$  shows a quasi-Toeplitz pattern due to the presence of obstruction, where the darker region corresponds to the obstructed region.

4) *Coexistence of LOS, Reflection, and Obstruction*: The scenario in Fig. 1 involves the simultaneous presence of LOS, reflection, and obstruction. In this case, the observed beam pattern can be interpreted as the superposition of contributions from the real BS  $s_0$  (without wall reflection) and its mirror BS  $s_1$  (modeling the wall reflection).

When considering only the propagation originating from BS  $s_0$ , the setting is identical to that in Section III-B3. Region  $\mathbf{G}_1$  corresponds to the unobstructed LOS region, whereas region  $\mathbf{G}_2$  represents the obstruction region where the direct path is blocked by the building.

For the propagation from the mirror BS  $s_1$ , shown in Fig. 5, the LOS, reflection, and obstruction effects coexist. The two regions  $\mathbf{G}_1$  and  $\mathbf{G}_2$  appear again, corresponding respectively to the mirror-LOS area with distance to  $s_1$  less than  $d_1$ , and the mirror-obstruction area with distance to  $s_1$  between  $d_1$  and  $d_2$ . In addition, a distinct region  $\mathbf{G}_3$  emerges, where the reflected

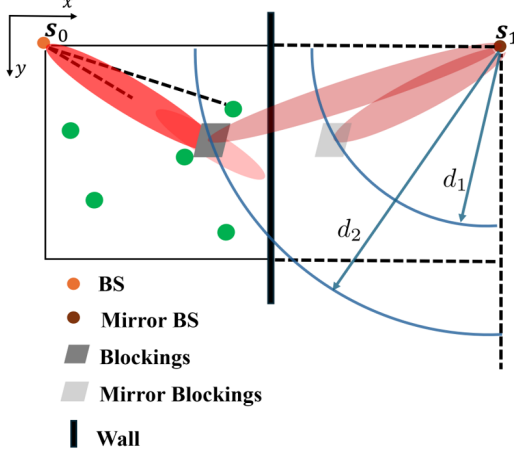


Figure 5. Propagation from the mirror BS  $s_1$  yields three distance regimes: (i) an LOS region for  $d \leq d_1$ ; (ii) a single-obstruction region for  $d_1 < d \leq d_2$ ; and (iii) a double-obstruction region for  $d > d_2$ .

path is simultaneously blocked by both the real building and its mirror image.

Following the same modeling principle as in Section III-B2, this scenario can be represented by (11) with  $R = 3$ .

Since the LOS and obstruction regions share the same spatial partitions  $\mathbf{G}_1$  and  $\mathbf{G}_2$  as their mirror counterparts, the corresponding attenuation components can be aggregated as

$$\rho_1 = \rho_1^{(0)} + \rho_1^{(1)}, \quad \rho_2 = \rho_2^{(0)} + \rho_2^{(1)}. \quad (16)$$

In contrast, region  $\mathbf{G}_3$  is affected solely by the mirror-induced double obstruction and therefore contains only the corresponding attenuation component  $\rho_3$ .

#### IV. TOEPLITZ-STRUCTURED MATRIX-VECTOR TENSOR DECOMPOSITION

In this section, we propose a matrix-vector tensor decomposition-based optimization formulation to reconstruct the general scenario where LOS, reflections, and obstructions coexist, as illustrated in Fig. 1. The relatively simpler propagation scenarios discussed in Sections III-B1–III-B3 can be addressed in a similar manner as special cases of the proposed formulation.

##### A. Matrix-Vector Tensor Decomposition Formulation

Building upon the coordinate transformation, the RSS measurements in the polar domain can be expressed using a multi-term matrix-vector tensor decomposition as given in (11). This representation allows the reconstruction task to be formulated as a constrained optimization problem, where the objective is to estimate the beam-space matrices  $\{\mathbf{G}_r\}$  and distance-domain attenuation vector  $\{\rho_r\}$  from the observed measurements while maintaining the underlying physical characteristics.

To obtain a physically consistent and structurally regularized representation, we exploit the near-Toeplitz structure of the beam-space gain matrices  $\mathbf{G}_r$ . Rather than enforcing a strict Toeplitz constraint, we incorporate a soft regularization term,

since in environments where both reflection and obstruction are present, the beam patterns only exhibit approximate shift-invariance, as discussed in Section III-B3. Moreover, because signal power decays with propagation distance, the nonzero portion of each attenuation profile  $\rho_r$  is assumed to be monotonically decreasing. These physical considerations directly motivate the regularization terms and constraints adopted in the reconstruction formulation.

Define  $\mathbf{W} \in \mathbb{R}^{I \times J \times K}$  as an indication tensor such that

$$[\mathbf{W}]_{i,j,k} = \begin{cases} 1, & \text{if } (i,j,k) \in \Omega \\ 0, & \text{otherwise} \end{cases}$$

where  $\Omega$  denotes the index set of UE measurements in the polar coordinate system. Then, the reconstruction of the MIMO beam map  $\mathbf{X}$  can be formulated as  $\mathcal{P}$

$$\mathcal{P}: \underset{\{\mathbf{G}_r\}, \{\rho_r\}}{\text{minimize}} \left\| \mathbf{W} * (\mathbf{X} - \left( \sum_{r=1}^R \mathbf{G}_r \circ \rho_r \right)) \right\|_F^2 \quad (17)$$

$$+ \sum_{r=1}^R \lambda_r \sum_{i=1}^{I-1} \sum_{j=1}^{J-1} |[\mathbf{G}_r]_{i,j} - [\mathbf{G}_r]_{i+1,j+1}|^2 \quad (18)$$

$$+ \lambda \|\mathbf{G}_1, \dots, \mathbf{G}_R\|_F^2 \quad (19)$$

$$\text{subject to } \rho_{r,k} \geq 0 \forall k, r \quad (20)$$

$$\sum_{r,k} \rho_{r,k} = 1 \quad (21)$$

$$\sum_r \rho_{r,k} \geq \sum_r \rho_{r,k+1} \quad \forall k = 1, \dots, K-1 \quad (22)$$

$$\rho_{1,k} \geq \rho_{1,k+1} \quad \forall k = 1, \dots, K-1 \quad (23)$$

$$[\mathbf{G}_r]_{i,j} > 0 \quad \forall i, j, r, \quad (24)$$

where ‘\*’ represents element-wise product. The term  $[\mathbf{G}_r]_{i,j} - [\mathbf{G}_r]_{i+1,j+1}$  serves as a Toeplitz regularization, the Frobenius norm  $\|\mathbf{G}_1, \dots, \mathbf{G}_R\|_F^2$  prevents overfitting by penalizing large magnitudes. Each power term  $\rho_r$  is constrained to be nonnegative as in (20) and normalized such that the total powers  $\rho_r$  satisfy (21) to ensure stable convergence. Since the index  $k$  corresponds to the distance, the total power should decay with  $k$  as in (22). Moreover, (23) guarantees that the first component’s power profile  $\rho_1$  decreases smoothly along the distance dimension. The same monotonicity constraint is not imposed on the other components  $\rho_r$ , as their profiles may contain zeros at small index  $k$  due to the presence of reflections and blockages.

To facilitate computation, let the matrix  $\underline{\mathbf{X}} \in \mathbb{R}^{(I \times J) \times K}$  and  $\underline{\mathbf{W}} \in \mathbb{R}^{(I \times J) \times K}$  represent the mode-3 unfolding of tensor  $\mathbf{X}$  and  $\mathbf{W}$ , respectively. The mode-3 unfolding is defined as

$$\underline{\mathbf{X}} = [\text{vec}(\mathbf{X}_{::,1}), \text{vec}(\mathbf{X}_{::,2}), \dots, \text{vec}(\mathbf{X}_{::,K})]$$

where  $\mathbf{X}_{::,k}$  is the  $k$ th slice of the tensor  $\mathbf{X}$ . Additionally, define the matrix  $\underline{\mathbf{G}} = [\text{vec}(\mathbf{G}_1), \dots, \text{vec}(\mathbf{G}_R)] \in \mathbb{R}^{(I \times J) \times R}$

and  $\boldsymbol{\varrho} = [\boldsymbol{\rho}_1, \dots, \boldsymbol{\rho}_R] \in \mathbb{R}^{K \times R}$ . Then, the problem  $\mathcal{P}$  can be rewritten as

$$\mathcal{P}' : \underset{\underline{\mathbf{G}}, \boldsymbol{\varrho}}{\text{minimize}} \|\underline{\mathbf{W}} * \underline{\mathbf{X}} - \underline{\mathbf{W}} * (\underline{\mathbf{G}} \boldsymbol{\varrho}^T)\|_F^2 \quad (25)$$

$$+ \sum_{r=1}^R \lambda_r \sum_{i=1}^{I-1} \sum_{j=1}^{J-1} |[\mathbf{G}_r]_{i,j} - [\mathbf{G}_r]_{i+1,j+1}|^2 \\ + \lambda \|\underline{\mathbf{G}}\|_F^2$$

$$\text{subject to } \rho_{k,r} \geq 0, \forall k = 1, \dots, K, r = 1, \dots, R \\ \sum_{k,r} \rho_{k,r} = 1 \\ \sum_r \rho_{k,r} \geq \sum_r \rho_{k+1,r} \forall k = 1, \dots, K-1 \\ \rho_{k,1} \geq \rho_{k+1,1} \forall k = 1, \dots, K-1.$$

### B. Alternating Updates under Structural Regularization

The problem  $\mathcal{P}'$  is separately convex with respect to  $\underline{\mathbf{G}}$  and  $\boldsymbol{\varrho}$  when the other variable is fixed. We therefore adopt an alternating minimization scheme to iteratively update  $\underline{\mathbf{G}}$  and  $\boldsymbol{\varrho}$  until convergence.

**Update of  $\underline{\mathbf{G}}$ :** Given  $\boldsymbol{\varrho}$ , the subproblem with respect to  $\underline{\mathbf{G}}$  is formulated as

$$\underset{\underline{\mathbf{G}}}{\text{minimize}} \|\underline{\mathbf{W}} * \underline{\mathbf{X}} - \underline{\mathbf{W}} * (\underline{\mathbf{G}} \boldsymbol{\varrho}^T)\|_F^2 \quad (26)$$

$$+ \sum_{r=1}^R \lambda_r \sum_{i=1}^{I-1} \sum_{j=1}^{J-1} |[\mathbf{G}_r]_{i,j} - [\mathbf{G}_r]_{i+1,j+1}|^2 \\ + \lambda \|\underline{\mathbf{G}}\|_F^2.$$

This subproblem is convex since all the terms are convex. Therefore, it can be efficiently solved using proximal gradient descent [31].

**Update of  $\boldsymbol{\varrho}$ :** Given  $\underline{\mathbf{G}}$ , the subproblem with respect to  $\boldsymbol{\varrho}$  is given by

$$\underset{\boldsymbol{\varrho}}{\text{minimize}} \|\underline{\mathbf{W}} * \underline{\mathbf{X}} - \underline{\mathbf{W}} * (\underline{\mathbf{G}} \boldsymbol{\varrho}^T)\|_F^2 \quad (27)$$

$$\text{subject to } \rho_{k,r} \geq 0, \forall k = 1, \dots, K, r = 1, \dots, R \\ \sum_{k,r} \rho_{k,r} = 1 \\ \sum_r \rho_{k,r} \geq \sum_r \rho_{k+1,r} \forall k = 1, \dots, K-1 \\ \rho_{k,1} \geq \rho_{k+1,1} \forall k = 1, \dots, K-1.$$

This subproblem is convex with respect to  $\boldsymbol{\varrho}$ . Since the objective function is quadratic and all constraints are linear, it constitutes a standard quadratic program that can be efficiently solved using interior-point methods [32].

Finally, the reconstructed tensor is obtained as  $\hat{\mathcal{X}} = \sum_{r=1}^R \hat{\mathbf{G}}_r \circ \hat{\boldsymbol{\rho}}_r$ .

### V. SIMPLIFIED MODEL FOR THE PURE LOS REGION

In this section, we show that in the pure LOS region, enforcing the symmetric Toeplitz structure as hard constraints leads to a simplified formulation of problem  $\mathcal{P}$ , with substantially reduced computational complexity compared to the regularized formulation.

#### A. Simplified Model

For pure LOS region illustrated in Fig. 3(a), the matrix-vector tensor decomposition problem  $\mathcal{P}'$  can be simplified and formulated as

$$\mathcal{P}'' : \underset{\underline{\mathbf{G}}, \boldsymbol{\varrho}}{\text{minimize}} \|\underline{\mathbf{W}} * \underline{\mathbf{X}} - \underline{\mathbf{W}} * (\text{vec}(\underline{\mathbf{G}}) \boldsymbol{\varrho}^T)\|_F^2$$

$$+ \lambda_1 \sum_{i=1}^{I-1} \sum_{j=1}^{J-1} |[\mathbf{G}]_{i,j} - [\mathbf{G}]_{i+1,j+1}|^2 \\ + \lambda_2 \sum_{i=1}^I \sum_{j=1}^J |[\mathbf{G}]_{i,j} - [\mathbf{G}]_{j,i}|^2$$

$$\text{subject to } \rho_k > \rho_{k+1} > 0, \forall k = 1, \dots, K-1 \\ \sum_k \rho_k = 1.$$

This formulation can be solved using a similar alternating optimization framework as that adopted for the general problem  $\mathcal{P}'$ .

Since there is only a LOS region, the Toeplitz and symmetric properties can be imposed as hard constraints rather than through regularization. Under these structural constraints, the matrix  $\underline{\mathbf{G}}$  can be fully characterized by a single row vector, thereby converting the reconstruction task into a constrained least-squares problem. This representation remains effective even under severe measurement sparsity.

By enforcing Toeplitz and symmetry constraints, the matrix-vector tensor decomposition for the LOS region can be formulated as

$$\mathcal{P}''' : \underset{\underline{\mathbf{G}}, \boldsymbol{\varrho}}{\text{minimize}} \|\underline{\mathbf{W}} * \underline{\mathbf{X}} - \underline{\mathbf{W}} * (\text{vec}(\underline{\mathbf{G}}) \boldsymbol{\varrho}^T)\|_F^2 \quad (28)$$

$$\text{subject to } [\mathbf{G}]_{i,j} = [\mathbf{G}]_{j,i}, [\mathbf{G}]_{i,j} = [\mathbf{G}]_{i+1,j+1} \\ i+1 \leq I, j+1 \leq J \\ \rho_k > \rho_{k+1} > 0, \forall k = 1, \dots, K-1 \\ \sum_k \rho_k = 1.$$

We employ an alternating minimization scheme to iteratively solve for  $\underline{\mathbf{G}}$  and  $\boldsymbol{\varrho}$ , as detailed below.

**Update of  $\boldsymbol{\varrho}$ :** Given  $\underline{\mathbf{G}}$ , we recall that  $\underline{\mathbf{X}} \in \mathbb{R}^{(I \times J) \times K}$  and  $\underline{\mathbf{W}} \in \mathbb{R}^{(J \times K) \times K}$  are the mode-3 unfoldings of  $\mathcal{X}$  and  $\mathcal{W}$  respectively.

Then, the problem (28) becomes

$$\underset{\boldsymbol{\varrho}}{\text{minimize}} \|\underline{\mathbf{W}} * \underline{\mathbf{X}} - \underline{\mathbf{W}} * (\text{vec}(\underline{\mathbf{G}}) \boldsymbol{\varrho}^T)\|_F^2 \quad (29)$$

$$\text{subject to } \mathbf{A} \boldsymbol{\varrho} > 0, \boldsymbol{\varrho} > 0, \mathbf{1}^T \boldsymbol{\varrho} = 1,$$

where  $\mathbf{1} \in \mathbb{R}^K$  is all-ones vector, and  $\mathbf{A} \in \mathbb{R}^{(K-1) \times K}$  is a constraint matrix defined as

$$\mathbf{A} = \begin{bmatrix} 1 & -1 & 0 & \cdots & 0 \\ 0 & 1 & -1 & \cdots & 0 \\ \vdots & \vdots & \vdots & \ddots & \vdots \\ 0 & 0 & \cdots & 1 & -1 \end{bmatrix}.$$

Using the identity  $\underline{\mathbf{W}} * (\text{vec}(\mathbf{G})\boldsymbol{\rho}^T) = \text{diag}(\text{vec}(\mathbf{G}))\underline{\mathbf{W}}\text{diag}(\boldsymbol{\rho})$ , the objective function in (29) can be expanded as

$$\begin{aligned} & \|\underline{\mathbf{W}} * \underline{\mathbf{X}} - \text{diag}(\text{vec}(\mathbf{G}))\underline{\mathbf{W}}\text{diag}(\boldsymbol{\rho})\|_F^2 \\ &= \sum_{i=1}^{I \times J} \sum_{k=1}^K ([\mathbf{W}]_{i,k} [\mathbf{X}]_{i,k} - \text{vec}(\mathbf{G})_i [\mathbf{W}]_{i,k} \rho_k)^2. \end{aligned}$$

This problem can be further reformulated into the standard quadratic programming form

$$\underset{\boldsymbol{\rho}}{\text{minimize}} \quad \boldsymbol{\rho}^T \mathbf{H} \boldsymbol{\rho} + \mathbf{c}^T \boldsymbol{\rho} \quad (30)$$

$$\text{subject to} \quad \mathbf{A}\boldsymbol{\rho} > 0, \quad \boldsymbol{\rho} > 0, \quad \mathbf{1}^T \boldsymbol{\rho} = 1,$$

where  $\mathbf{H}$  is diagonal matrix with  $[\mathbf{H}]_{k,k} = 2 \sum_{i=1}^{I \times J} (\text{vec}(\mathbf{G})_i [\mathbf{W}]_{i,k})^2$ , and  $\mathbf{c} \in \mathbb{R}^K$  is given by  $c_k = -2 \sum_{i=1}^{I \times J} [\mathbf{W}]_{i,k} [\mathbf{X}]_{i,k} \text{vec}(\mathbf{G})_i$ .

This quadratic programming problem with a quadratic objective function and linear inequality constraints can be solved via interior-point method [32].

**Update of  $\mathbf{G}$ :** Given  $\boldsymbol{\rho}$ , problem (28) becomes

$$\begin{aligned} & \underset{\mathbf{G}}{\text{minimize}} \quad \|\mathbf{W} * (\mathbf{X} - (\mathbf{G} \circ \boldsymbol{\rho}))\|_F^2 \quad (31) \\ & \text{subject to} \quad [\mathbf{G}]_{i,j} = [\mathbf{G}]_{j,i}, \quad [\mathbf{G}]_{i,j} = [\mathbf{G}]_{i+1,j+1} \\ & \quad i+1 \leq I, j+1 \leq J. \end{aligned}$$

Under these hard constraints, matrix  $\mathbf{G}$  is a symmetric Toeplitz matrix. Recall that we consider a square grid with  $I = J \triangleq N$ . Matrix  $\mathbf{G}$  is fully determined by its first row  $\mathbf{g} = [g_0, g_1, \dots, g_{N-1}]^T$  and  $[\mathbf{G}]_{i,j} = g_{|i-j|}$ . Let  $\mathbf{T} \in \mathbb{R}^{N^2 \times N}$  denote the fixed transformation matrix such that  $\text{vec}(\mathbf{G}) = \mathbf{T}\mathbf{g} \in \mathbb{R}^{N^2}$ . Substituting this relation into the unfolded objective function (31) gives

$$\underset{\mathbf{g}}{\text{minimize}} \quad \|\underline{\mathbf{W}} * \underline{\mathbf{X}} - \text{diag}(\mathbf{T}\mathbf{g})\underline{\mathbf{W}}\text{diag}(\boldsymbol{\rho})\|_F^2. \quad (32)$$

Define  $\mathbf{y} = \text{vec}(\underline{\mathbf{W}} * \underline{\mathbf{X}})$ , and construct a matrix  $\mathbf{D} \in \mathbb{R}^{(N^2 \times K) \times N}$  such that  $[\mathbf{D}]_{(i-1) \times K+k, j} = T_{ij} [\mathbf{W}]_{i,k} \rho_k$ . Then, (32) reduces to the standard least-squares problem

$$\underset{\mathbf{g}}{\text{minimize}} \quad \|\mathbf{y} - \mathbf{D}\mathbf{g}\|_2^2. \quad (33)$$

This is an unconstrained strictly convex problem. Setting the first-order derivative to zero yields the closed-form solution

$$\hat{\mathbf{g}} = (\mathbf{D}^T \mathbf{D})^{-1} \mathbf{D}^T \mathbf{y}. \quad (34)$$

The matrix  $\mathbf{G}$  is then reconstructed as  $[\mathbf{G}]_{i,j} = \hat{g}_{|i-j|}$ .

Finally, the reconstructed MIMO beam map is obtained as  $\mathbf{X} = \hat{\mathbf{G}} \circ \hat{\boldsymbol{\rho}}$ .

The experimental comparison between the regularized and hard-constrained formulations is presented in Fig. 6, and discussed in detail in Section VI-A1.

## B. Complexity Analysis

In this subsection, we compare the computational complexity of the *regularized* formulation in  $\mathcal{P}''$  and the *hard-constrained* formulation in  $\mathcal{P}'''$  for the pure LOS case.

Both  $\mathcal{P}''$  and  $\mathcal{P}'''$  are solved by alternating minimization between vector  $\boldsymbol{\rho}$  and matrix  $\mathbf{G}$ . Let  $T_{\text{alt}}$  denote the number

of outer alternating iterations. In addition, let  $T_{\text{ip}}$  denote the number of Newton steps used by the interior-point solver for (30), and let  $T_{\text{pg}}$  denote the number of proximal-gradient iterations used to update  $\mathbf{G}$  in the regularized method.

1) *Update of  $\boldsymbol{\rho}$  (Common to  $\mathcal{P}''$  and  $\mathcal{P}'''$ )*: Given  $\mathbf{G}$ , updating  $\boldsymbol{\rho}$  yields a  $K$ -variable quadratic program with linear constraints. The coefficients  $\mathbf{H}$  and  $\mathbf{c}$  in (29) can be formed by accumulating only over observed entries, which costs  $\mathcal{O}(|\Omega|)$ . Solving the quadratic program via an interior-point method typically costs  $\mathcal{O}(T_{\text{ip}} K^3)$  [32]. Hence, the per-outer-iteration cost of the  $\boldsymbol{\rho}$ -update (30) is  $\mathcal{O}(|\Omega| + T_{\text{ip}} K^3)$ .

2) *Update of  $\mathbf{G}$ :* In  $\mathcal{P}''$ ,  $\mathbf{G} \in \mathbb{R}^{N \times N}$  contains  $N^2$  free variables and is estimated by minimizing a data-fitting term plus non-smooth structural regularizers. As described in Section IV-B, this subproblem can be solved by proximal-gradient descent. In each proximal-gradient iteration, computing the gradient of the quadratic data-fitting term can be implemented over the observed set, at a cost of  $\mathcal{O}(|\Omega|)$ , while evaluating the proximal mapping associated with the structural regularizers requires operations over all  $N^2$  entries (cost  $\mathcal{O}(N^2)$  per iteration). Therefore, the per-outer-iteration complexity of the  $\mathbf{G}$ -update in  $\mathcal{P}''$  is  $\mathcal{O}(T_{\text{pg}}(|\Omega| + N^2))$ .

In  $\mathcal{P}'''$ , symmetry and Toeplitz are imposed as hard constraints, so  $\mathbf{G}$  is fully determined by its first row  $\mathbf{g} = [g_0, g_1, \dots, g_{N-1}]^T \in \mathbb{R}^N$  with  $[\mathbf{G}]_{ij} = g_{|i-j|}$ , reducing the degrees of freedom from  $N^2$  to  $N$ . Given  $\boldsymbol{\rho}$ , the  $\mathbf{g}$ -update reduces to a least-squares problem (34). Since the value at any position  $(i, j)$  depends solely on the index difference  $|i - j|$ , each observation contributes to the estimation of a unique coefficient  $g_{|i-j|}$  without coupling with others. This structural orthogonality renders the Gram matrix  $\mathbf{D}^T \mathbf{D}$  diagonal, allowing  $\mathbf{g}$  to be computed efficiently by simple grouped accumulations over  $\Omega$ . Thus, the complexity is  $\mathcal{O}(|\Omega| + N)$ .

3) *Overall complexity*: Combining the above, the overall complexities are summarized as

$$\mathcal{P}'' : \mathcal{O}\left(T_{\text{alt}}\left(|\Omega| + T_{\text{ip}} K^3 + T_{\text{pg}}(|\Omega| + N^2)\right)\right), \quad (35)$$

$$\mathcal{P}''' : \mathcal{O}\left(T_{\text{alt}}\left(|\Omega| + T_{\text{ip}} K^3 + (|\Omega| + N)\right)\right). \quad (36)$$

In sparse-sampling regimes, the dominant difference stems from the spatial update:  $\mathcal{P}''$  optimizes over  $N^2$  unknowns and requires iterative proximal updates with per-iteration cost scaling as  $|\Omega| + N^2$ , whereas  $\mathcal{P}'''$  reduces the spatial degrees of freedom to  $N$  and admits a least-squares update that scales primarily with the number of observations  $|\Omega|$ .

## VI. NUMERICAL RESULTS

In this section, we use the models in (2) and (3) to simulate the MIMO beam map over an  $L \times L$  area with  $L = 48$  meters. The BS is located at  $\mathbf{s}_0 = (0, 0)$ , and we set the number of antennas to  $N_t = 16$ . The large-scale fading coefficients are chosen as  $\alpha_0 = d^\eta$  and  $\alpha_1 = d^\eta/2$  where  $d = \|\mathbf{z} - \mathbf{s}_0\|_2$ . The path-loss exponent is set to  $\eta = -2$  for unobstructed propagation and  $\eta = -6$  when the path is blocked. The noise terms  $n^{(0)}$  and  $n^{(1)}$  are modeled with standard deviations  $\sigma_0 = 3\text{dB}$  and  $\sigma_1 = 1\text{dB}$ . We choose the dimension of  $\mathbf{X}$  to be  $I = J = 46$  and  $K = 40$ . The beam angles  $\{\theta_i\}_{i=1}^I$  are generated

such that  $\sin \theta_i$  is uniformly spaced over  $[\sin \theta_1, \sin \theta_I]$ , where  $\theta_1 = 0.0208$  and  $\theta_I = 1.55$ . The spatial angle  $\phi_j$  is chosen to be the same as  $\theta_i$  to satisfy Lemma 1.

As illustrated in Fig. 1, a wall is assumed to exist along the right-hand side of the region, connecting the vertices  $(48, 0)$  and  $(48, 48)$ . The corresponding mirror BS for the reflected path is therefore located at  $s_1 = (96, 0)$ . UE locations are drawn uniformly at random in the  $L \times L$  area to obtain RSS  $\gamma_{m,i}^{(0)}$  and  $\gamma_{m,i}^{(1)}$ .

We first transform the measurements  $\{(\theta_i, z_m, \gamma_{m,i})\}$  into the polar coordinate system  $(\phi, d)$  via (6). The proposed Toeplitz-structured matrix-vector tensor decomposition method is then applied to reconstruct the MIMO beam map  $\mathcal{X}$  under the polar coordinate system. After decomposition,  $\mathcal{X}$  needs to be mapped back to the Cartesian coordinate system to obtain MIMO beam map  $\mathcal{Y} \in \mathbb{R}^{L \times L \times I}$  to convey direct beam information. Each entry  $[\mathcal{X}]_{i,j,k}$  indexed by  $(\theta_i, \phi_j, d_k)$ , is converted to a corresponding Cartesian location  $z_{m_0}$ , where  $m_0 = 1, \dots, M_0$ , and  $M_0 = K \times J$ . This is because under a fixed beam  $\theta_i$ , the number of values in  $\mathcal{X}_{i,:,:}$  is  $K \times J$ . Denote  $\gamma_{m_0}$  as a one-to-one mapping to  $\mathcal{X}_{i,j,k}$  at  $z_{m_0}$ . Then, the set of measurements becomes  $\{(\theta_i, z_{m_0}, \gamma_{m_0})\}$ . It is noted that under a fixed  $\theta_i$ , there is a beam-space matrix  $\mathcal{Y}_{i,:,:} \in \mathbb{R}^{L \times L}$ . We propose to interpolate such matrix  $\mathcal{Y}_{i,:,:}$  for each  $\theta_i$  based on the measurements  $\{(\theta_i, z_{m_0}, \gamma_{m_0})\}$  using thin plate spline (TPS). The reconstruction performance is evaluated using the normalized mean squared error (NMSE), defined as  $\|\mathcal{Y} - \hat{\mathcal{Y}}\|_F^2 / \|\mathcal{Y}\|_F^2$ .

We compare the proposed Toeplitz-structured matrix-vector tensor decomposition approach with the following baseline methods:

- Baseline 1: The  $k$ -nearest neighbors (KNN) method, with  $k = 3$ .
- Baseline 2: The TPS [33], applied independently for each beam  $\theta_i$  to construct the corresponding 2D beam map from the measurements  $\{(\theta_i, z_m, \gamma_{m,i})\}$ .
- Baseline 3: The traditional block-term tensor decomposition (BTD) [20] method without imposing Toeplitz structure.

Note that low-rank tensor completion [34] exhibits significantly degraded performance under highly sparse observations and is therefore excluded from comparison. Baselines 1 and 2 are purely 2D interpolation methods and reconstruct the MIMO beam map for each beam angle  $\theta_i$  independently, without exploiting any structural correlations.

#### A. Simulation for Pure LOS Scenario

In this subsection, we show the simulation results under a LOS scenario in Fig. 3(a).

1) *Comparison between Toeplitz Constraint and Toeplitz Regularization:* We compare the NMSE performance of reconstructing  $\mathcal{X}$  using the Toeplitz constraint formulation in problem  $\mathcal{P}'''$  and the Toeplitz regularization formulation in problem  $\mathcal{P}''$ . Fig. 6 reports the NMSE under different sampling ratios, where the Toeplitz constraint method consistently achieves lower NMSE than the regularization-based counterpart across all sampling rates. The improvement

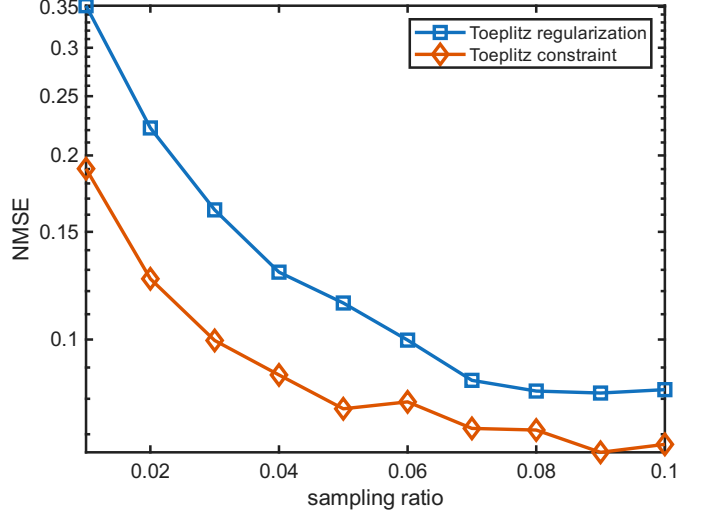


Figure 6. NMSE comparison between the Toeplitz constraint and Toeplitz regularization methods under different sampling ratios. The constraint method performs better than using Toeplitz as regularization.

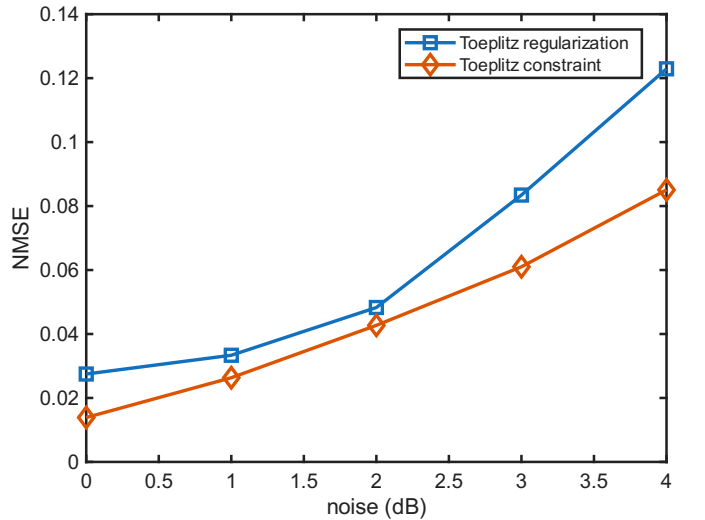


Figure 7. NMSE comparison between the Toeplitz constraint and Toeplitz regularization methods under different noise. The constraint method performs better than using Toeplitz as regularization.

is more pronounced in the low-sampling regime, indicating that directly enforcing the Toeplitz structure is particularly beneficial when measurements are sparse.

To further evaluate robustness, Fig. 7 shows the NMSE under different noise levels from 0 to 4 dB. As the noise increases, the NMSE of both methods degrades, but the Toeplitz constraint method maintains a clear performance advantage throughout the tested SNR range. Overall, these results suggest that when the Toeplitz prior accurately matches the underlying signal structure in the pure LOS case, hard structural enforcement yields more reliable reconstructions than soft regularization, and remains consistently superior under both sampling ratios variation and noise perturbation.

2) *The Performance under Different Sampling Ratios:* We evaluate the performance of the proposed method for reconstructing  $\mathcal{Y}$  under sampling ratios  $r_s = 0.04 - 0.1$ . The

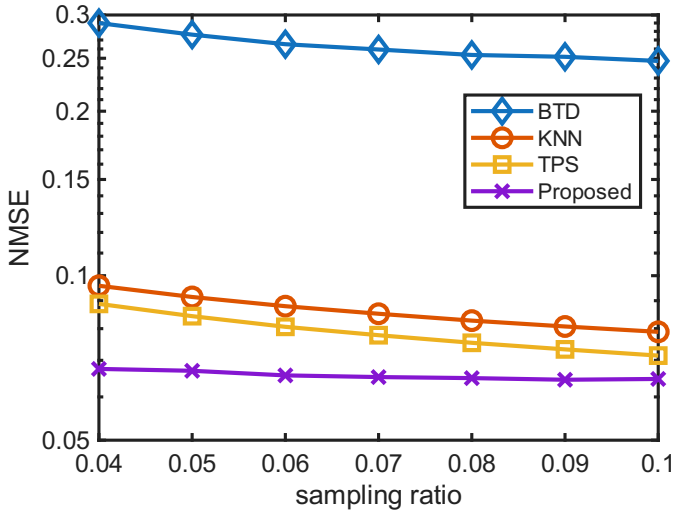


Figure 8. Reconstruction NMSE of  $\mathcal{Y}$  of LOS scenario under different sampling ratios

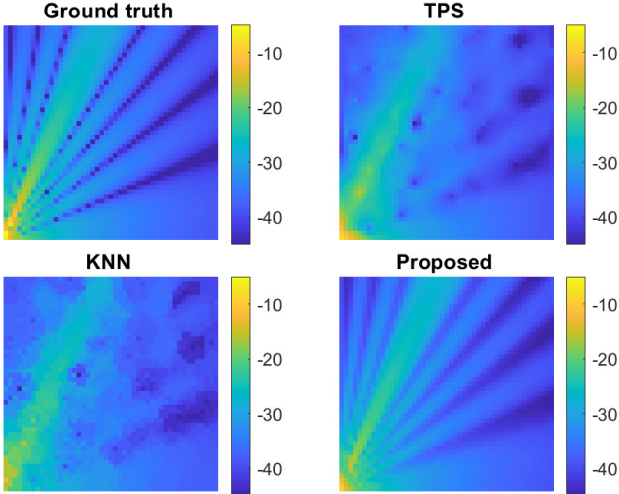


Figure 9. Visual comparison of the reconstructed direct beam map at sampling ratio  $r_s = 0.1$ . The proposed method successfully captures the beam pattern, while TPS and KNN produce blurred and inaccurate reconstructions.

NMSE results are presented in Fig. 8. The proposed method consistently outperforms all baseline approaches, achieving more than a 20% improvement at low sampling ratios. The traditional BTD method fails to recover the MIMO beam map because it does not exploit the Toeplitz structure. The TPS and KNN interpolation methods also perform poorly, as they cannot capture the underlying beam pattern.

To further illustrate the reconstruction quality, we set the sampling ratio to  $r_s = 0.1$  and show the visual results in Fig. 9. The proposed method accurately reconstructs the MIMO beam map by leveraging the Toeplitz structure, while TPS and KNN can only provide coarse approximations and fail to recover the fine beam features.

#### B. Simulation for Coexistence of LOS and Reflection

In this subsection, we examine the reconstruction performance when LOS and reflection coexist.

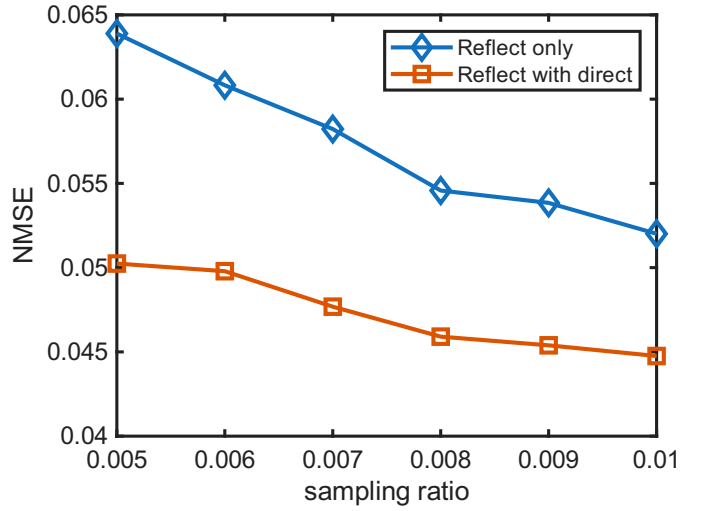


Figure 10. Reconstruction NMSE comparison showing the benefit of incorporating direct-path measurements when reconstructing the reflected beam using the matrix-vector tensor formulation.

1) *Benefits of the Matrix-Vector Tensor Decomposition for Reflected-Beam Reconstruction:* We demonstrate that the measurements from the direct-path beam can improve the reconstruction of the reflected-path beam through the proposed matrix-vector tensor formulation in (12). In Fig. 10, the method “Reflect only” uses only the reflection measurements to reconstruct the MIMO beam map associated with the mirror BS  $s_1$ . In contrast, the method “Reflect with direct” jointly incorporates both the LOS and reflection measurements using the tensor formulation introduced in (12).

As shown in Fig. 10, the joint formulation achieves more than a 10% improvement in NMSE. This gain arises because the LOS and reflected beams share the same intrinsic energy distribution  $\mathbf{G}$ . Therefore, the LOS measurements provide additional information that helps estimate  $\mathbf{G}$  more accurately, which in turn benefits the reconstruction of the reflected beam.

2) *The Performance under Different Sampling Ratios:* Here, similar to the LOS scenario, we evaluate the proposed method under sampling ratios  $r_s = 0.04 - 0.1$  for reconstructing  $\mathcal{Y}$ . Since the direct-beam result is similar to the LOS case in Section VI-A, we focus on the reconstruction NMSE of the whole MIMO beam map (the aggregate of direct and reflected beams), as shown in Fig. 11. The proposed method achieves over a 20% improvement in NMSE compared with all baseline methods, as illustrated in Fig. 11.

We further set the sampling ratio to  $r_s = 0.1$  and visualize the reconstruction results for the reflected beam and the whole MIMO beam map in Fig. 12 and Fig. 13, respectively. The proposed method accurately reconstructs both components, whereas TPS and KNN produce only coarse approximations and fail to capture the underlying beam patterns.

#### C. Simulation for Coexistence of LOS and Obstruction

In this subsection, we examine the reconstruction performance when the direct path is obstructed by a building located within the area of interest, as illustrated in Fig. 3(c). The polygonal coordinates of the building are given by

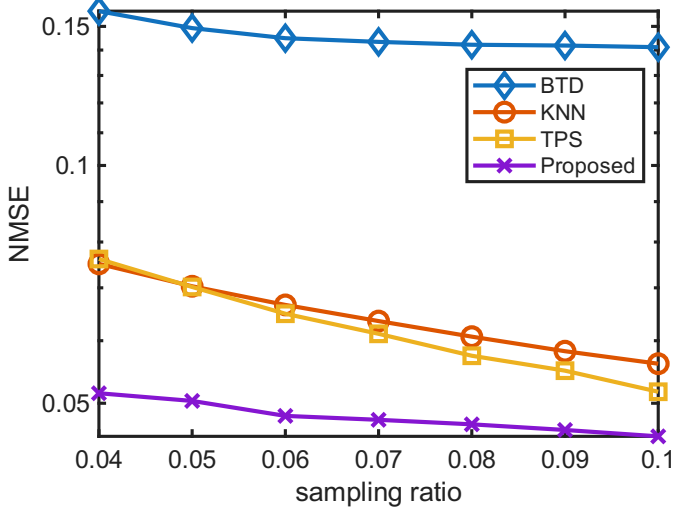


Figure 11. Reconstruction NMSE of  $\mathcal{Y}$  for the coexistence of LOS and reflection scenario under different sampling ratios.

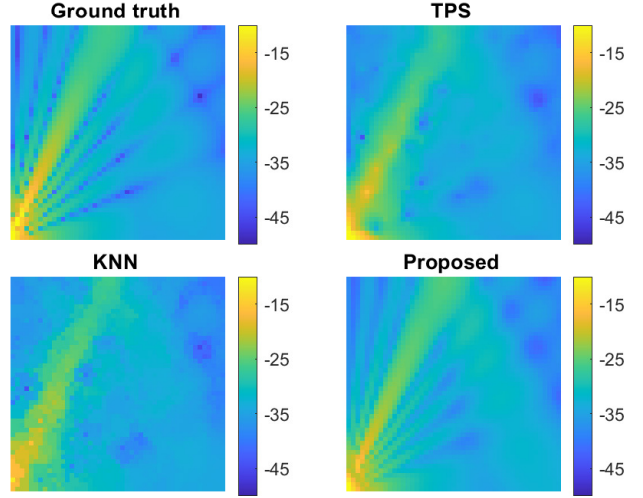


Figure 13. Visual comparison of reconstructed whole MIMO beam map (LOS + reflection) at sampling ratio  $r_s = 0.1$ . The proposed method reconstructs the beam structure faithfully, outperforming TPS and KNN.

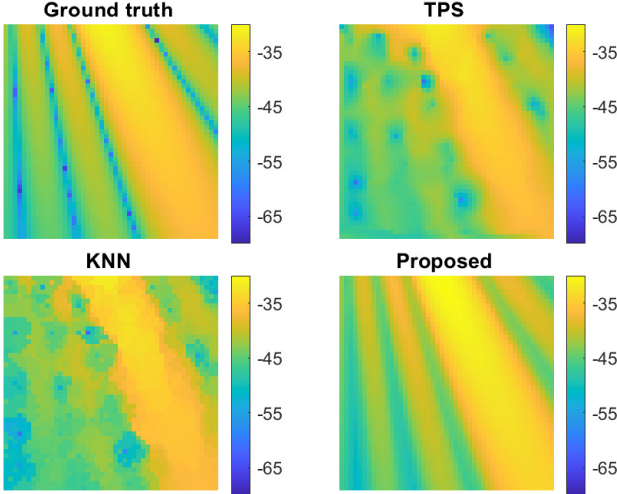


Figure 12. Visual comparison of the reconstructed reflected beam map at sampling ratio  $r_s = 0.1$ . The proposed method successfully captures the reflected-beam pattern, while TPS and KNN produce blurred and inaccurate reconstructions.

$\{(32, 26), (26, 32), (30, 38), (38, 32)\}$ . We evaluate the proposed method under different sampling ratios  $r_s = 0.04 - 0.1$  for reconstructing  $\mathcal{Y}$ . The NMSE results are presented in Fig. 14. It can be observed that the proposed method consistently outperforms baselines KNN and TPS, achieving more than 40% improvement in reconstruction accuracy across all sampling ratios. The superiority of the proposed method is mainly due to its structured tensor formulation: it enforces near-Toeplitz angular patterns and monotone distance-dependent attenuation through  $\{\mathbf{G}_r\}$  and  $\{\rho_r\}$ , which allows the model to reconstruct both the LOS region and the shadowed region with few samples while preserving the sharp power drop at the blockage. TPS, with its global smoothness prior, oversmooths this drop, and KNN suffers from unreliable local averaging near sparsely sampled blocked areas.

To further illustrate the reconstruction quality, we set the

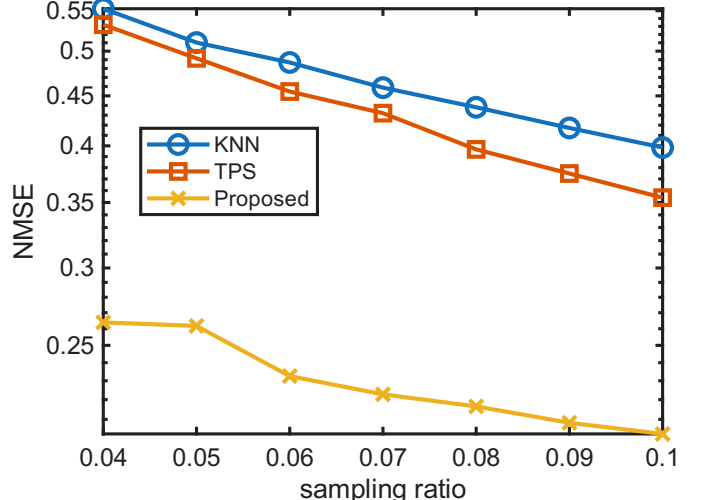


Figure 14. Reconstruction NMSE of  $\mathcal{Y}$  under the coexistence of LOS and obstruction. The proposed method consistently achieves lower NMSE than the KNN and TPS baselines across all sampling ratios, demonstrating a clear advantage in handling the mixed propagation scenario.

sampling ratio to  $r_s = 0.1$  and present the visual comparisons in Fig. 15. The proposed method better preserves the spatial pattern and partially restores the blocked region, whereas TPS and KNN produce distorted results. The corner region remains difficult to recover due to the absence of measurements.

#### D. Simulation for Coexistence of LOS, Reflection and Obstruction

In this subsection, we examine the reconstruction performance when both direct and reflected paths exist with obstruction, as illustrated in Fig. 4. To model the reflected path, a mirror building is generated by mirroring the real building with respect to the wall, with coordinates  $\{(32, 70), (26, 64), (30, 58), (38, 64)\}$ .

We evaluate the proposed method under different sampling ratios  $r_s = 0.1 - 0.2$  for reconstructing  $\mathcal{Y}$ . The NMSE

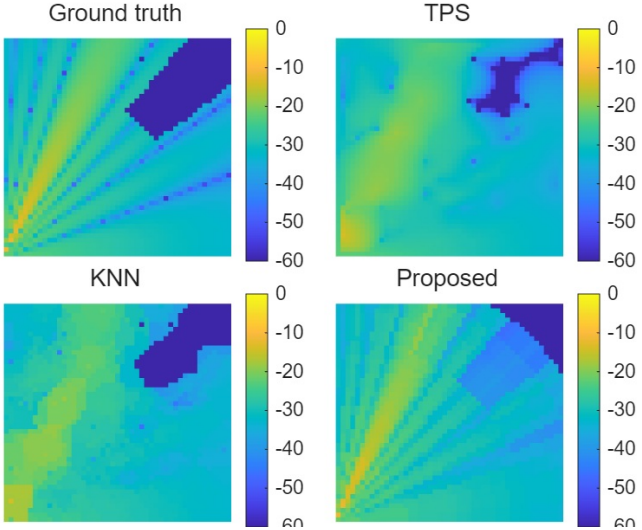


Figure 15. Visual comparison of reconstructed MIMO beam map (LOS + obstruction) at sampling ratio  $r_s = 0.1$ . The proposed method better preserves the overall spatial pattern and partially recovers the blocked region, whereas TPS and KNN produce distorted or over-smoothed reconstructions.

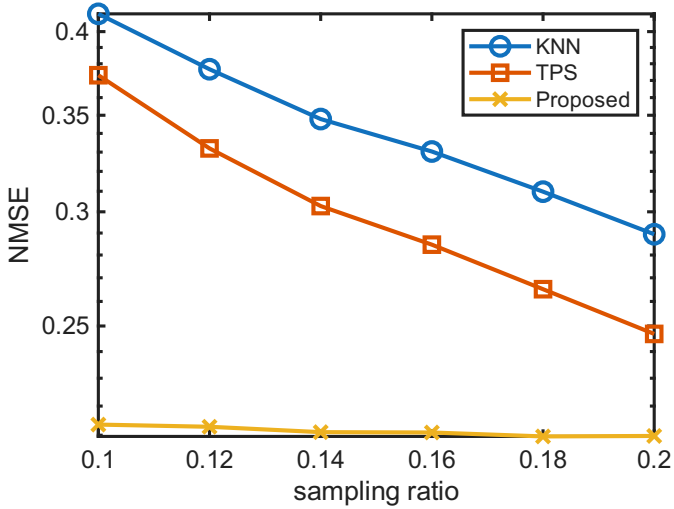


Figure 16. Reconstruction NMSE of  $\mathcal{Y}$  under the coexistence of LOS, reflection and obstruction. The proposed method consistently achieves lower NMSE than the KNN and TPS baselines across all sampling ratios, demonstrating a clear advantage in handling the mixed propagation scenario.

results are presented in Fig. 16. It can be observed that the proposed method consistently outperforms baselines KNN and TPS, achieving more than 20% improvement in reconstruction accuracy under low sampling ratios.

To further illustrate the reconstruction quality, we set the sampling ratio to  $r_s = 0.1$  and present the visual comparisons in Fig. 17. The proposed method better preserves the spatial pattern and partially restores the blocked region, whereas TPS and KNN produce distorted results.

## VII. CONCLUSION

This paper proposed a structure-aware approach for reconstructing MIMO beam map from sparse measurements.

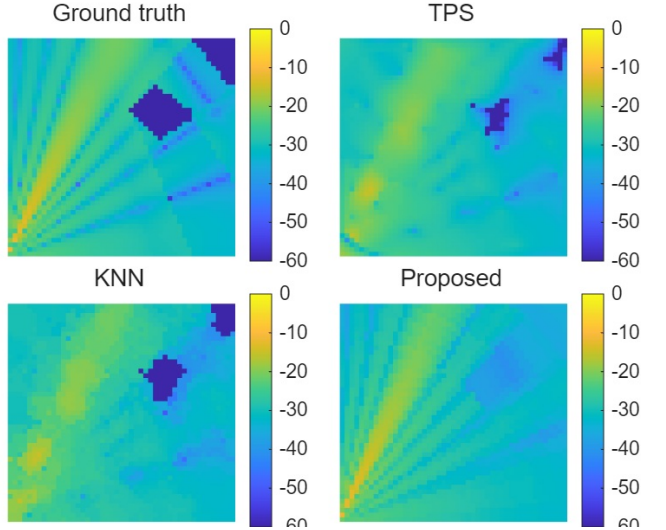


Figure 17. Visual comparison of reconstructed MIMO beam map (LOS + reflection + obstruction) at sampling ratio  $\rho = 0.1$ . The proposed method better preserves the overall spatial pattern and partially recovers the blocked region, whereas TPS and KNN produce distorted or over-smoothed reconstructions.

By transforming Cartesian observations into a polar coordinate system, we revealed a matrix and vector outer-product structure associated with different propagation conditions. The matrix representing beam-space gain was shown to have an intrinsic Toeplitz pattern, while the vector captured distance-dependent attenuation. Leveraging these properties, we developed a Toeplitz-structured matrix-vector tensor decomposition framework and an alternating minimization algorithm for efficient reconstruction. Simulation results confirmed that the proposed method achieves more than 20% improvement in reconstruction NMSE across a wide range of sampling ratios, outperforming interpolation methods and conventional BTD models. These results highlight the effectiveness of leveraging the latent angular and radial structure embedded in MIMO beam map.

## APPENDIX A PROOF OF LEMMA 1

Since  $\sin(\theta_i) = i/I$ ,  $\sin(\phi_j) = j/J$ , and  $I = J$ , the difference between the sine terms depends solely on the index difference. Specifically, for any integer shift  $\delta$  such that indices  $i + \delta$  and  $j + \delta$  are valid, we have

$$\begin{aligned} & \sin(\theta_{i+\delta}) - \sin(\phi_{j+\delta}) \\ &= \frac{i + \delta}{I} - \frac{j + \delta}{I} \\ &= \frac{i - j}{I} = \sin(\theta_i) - \sin(\phi_j). \end{aligned} \quad (37)$$

Then, under (37), we examine the difference between diagonal-shifted entries

$$\begin{aligned} & [\mathbf{G}]_{i,j} - [\mathbf{G}]_{i+\delta,j+\delta} \\ &= \left( \left| \sum_{n=0}^{N_t-1} \exp^{j\pi n(\sin(\theta_i) - \sin(\phi_j))} \right|^2 \right. \end{aligned}$$

$$= 0.$$

$$-\left| \sum_{n=0}^{N_t-1} \exp^{j\pi n(\sin(\theta_{i+\delta}) - \sin(\phi_{j+\delta}))} \right|^2$$

This implies that matrix  $\mathbf{G}$  has a Toeplitz structure.

For the symmetric property, we compare  $[\mathbf{G}]_{i,j}$  and  $[\mathbf{G}]_{j,i}$ . Note that

$$\sin(\theta_j) - \sin(\phi_i) = \frac{j-i}{I} = -(\sin(\theta_i) - \sin(\phi_j)). \quad (38)$$

Thus, the entry  $[\mathbf{G}]_{j,i}$  can be written as

$$[\mathbf{G}]_{j,i} = \left| \sum_{n=0}^{N_t-1} \exp(j\pi n(\sin(\theta_j) - \sin(\phi_i))) \right|^2$$

$$= \left| \sum_{n=0}^{N_t-1} \exp(-j\pi n(\sin(\theta_i) - \sin(\phi_j))) \right|^2. \quad (39)$$

Let  $z = \sum_{n=0}^{N_t-1} \exp(j\pi n(\sin(\theta_i) - \sin(\phi_j)))$ . The expression for  $[\mathbf{G}]_{j,i}$  corresponds to  $|z|^2$  (where  $\bar{z}$  is the complex conjugate of  $z$ ). Using the property that  $|z| = |\bar{z}|$  for any complex number, we have

$$[\mathbf{G}]_{i,j} - [\mathbf{G}]_{j,i} = |z|^2 - |\bar{z}|^2 = 0. \quad (40)$$

This concludes that  $\mathbf{G}$  is symmetric.

## REFERENCES

- [1] Q. Xue, C. Ji, S. Ma, J. Guo, Y. Xu, Q. Chen, and W. Zhang, "A survey of beam management for mmWave and THz communications towards 6G," *IEEE Commun. Surv. Tutor.*, vol. 26, no. 3, pp. 1520–1559, Feb. 2024.
- [2] J. Brady, N. Behdad, and A. M. Sayeed, "Beamspace MIMO for millimeter-wave communications: System architecture, modeling, analysis, and measurements," *IEEE Trans. Antennas Propag.*, vol. 61, no. 7, pp. 3814–3827, Jul. 2013.
- [3] X. Yu, J. Zhang, M. Haenggi, and K. B. Letaief, "Coverage analysis for millimeter wave networks: The impact of directional antenna arrays," *IEEE J. Sel. Areas Commun.*, vol. 35, no. 7, pp. 1498–1512, Apr. 2017.
- [4] W. Chen, J. Chen, and S. Cui, "Physics-informed neural networks for MIMO beam map and environment reconstruction," 2025. [Online]. Available: <https://arxiv.org/abs/2510.21238>
- [5] H. Wang, X. Shi, H. Zhang, Y. Cao, S. Yang, J. Wang, and K. Huang, "BeamCKM: A framework of channel knowledge map construction for multi-antenna systems," 2025. [Online]. Available: <https://arxiv.org/abs/2511.18376>
- [6] T. N. Ha, D. Romero, and R. Lopez-Valcarce, "Radio maps for beam alignment in mmwave communications with location uncertainty," in *2024 IEEE 99th Vehicular Technology Conference (VTC2024-Spring)*, Singapore, 2024, pp. 1–7.
- [7] T.-H. Chou, N. Michelusi, D. J. Love, and J. V. Krogmeier, "Fast position-aided mimo beam training via noisy tensor completion," *IEEE J. Sel. Top. Signal Process.*, vol. 15, no. 3, pp. 774–788, Mar. 2021.
- [8] L. Ma, Y. Fan, Y. Xu, and Y. Cui, "Pedestrian dead reckoning trajectory matching method for radio map crowdsourcing building in wifi indoor positioning system," in *Proc. IEEE Int. Conf. Commun.* IEEE, Paris, France, 2017, pp. 1–6.
- [9] W. B. Chikha, M. Masson, Z. Altman, and S. B. Jemaa, "Radio environment map based inter-cell interference coordination for massive-MIMO systems," *IEEE Trans. Mob. Comput.*, vol. 23, no. 1, pp. 785–796, Jan. 2024.
- [10] W. Feng, Y. Lin, Y. Wang, J. Wang, Y. Chen, N. Ge, S. Jin, and H. Zhu, "Radio map-based cognitive satellite-UAV networks towards 6G on-demand coverage," *IEEE Trans. Cogn. Commun. Netw.*, vol. 10, no. 3, pp. 1075–1089, Jun. 2024.
- [11] Y. Zeng, J. Chen, J. Xu, D. Wu, X. Xu, S. Jin, X. Gao, D. Gesbert, S. Cui, and R. Zhang, "A tutorial on environment-aware communications via channel knowledge map for 6G," *IEEE Commun. Surv. Tutor.*, vol. 26, no. 3, pp. 1478–1519, Feb. 2024.
- [12] K. Sato, K. Suto, K. Inage, K. Adachi, and T. Fujii, "Space-frequency-interpolated radio map," *IEEE Trans. Veh. Technol.*, vol. 70, no. 1, pp. 714–725, Jan. 2021.
- [13] A. Verdin, C. Funk, B. Rajagopalan, and W. Kleiber, "Kriging and local polynomial methods for blending satellite-derived and gauge precipitation estimates to support hydrologic early warning systems," *IEEE Trans. Geosci. Remote Sens.*, vol. 54, no. 5, pp. 2552–2562, Jan. 2016.
- [14] J. Fan, *Local polynomial modelling and its applications: Monographs on statistics and applied probability* 66. Routledge, 1996.
- [15] M. Hamid and B. Beferrull-Lozano, "Non-parametric spectrum cartography using adaptive radial basis functions," in *Proc. IEEE Int. Conf. Acoustics, Speech, Signal Processing*, 2017, pp. 3599–3603.
- [16] J. Wang, Q. Zhu, Z. Lin, J. Chen, G. Ding, Q. Wu, G. Gu, and Q. Gao, "Sparse bayesian learning-based hierarchical construction for 3D radio environment maps incorporating channel shadowing," *IEEE Trans. Wireless Commun.*, vol. 23, no. 10, pp. 14560–14574, Oct. 2024.
- [17] J. Wang, Q. Zhu, Z. Lin, Q. Wu, Y. Huang, X. Cai, W. Zhong, and Y. Zhao, "Sparse bayesian learning-based 3D radio environment map construction-sampling optimization, scenario-dependent dictionary construction, and sparse recovery," *IEEE Trans. Cogn. Commun. Netw.*, vol. 10, no. 1, pp. 80–93, Oct. 2024.
- [18] S.-J. Kim and G. B. Giannakis, "Cognitive radio spectrum prediction using dictionary learning," in *Proc. IEEE Global Telecomm. Conf.*, Atlanta, GA, USA, Jun. 2013, pp. 3206–3211.
- [19] H. Sun and J. Chen, "Propagation map reconstruction via interpolation assisted matrix completion," *IEEE Trans. Signal Process.*, vol. 70, pp. 6154–6169, Dec. 2022.
- [20] G. Zhang, X. Fu, J. Wang, X.-L. Zhao, and M. Hong, "Spectrum cartography via coupled block-term tensor decomposition," *IEEE Trans. Signal Process.*, vol. 68, pp. 3660–3675, May 2020.
- [21] X. Chen, J. Wang, and Q. Huang, "Dynamic spectrum cartography: Reconstructing spatial-spectral-temporal radio frequency map via tensor completion," *IEEE Trans. Signal Process.*, vol. 73, pp. 1184–1199, Jan. 2025.
- [22] Y. Teganya and D. Romero, "Deep completion autoencoders for radio map estimation," *IEEE Trans. Wireless Commun.*, vol. 21, no. 3, pp. 1710–1724, Mar. 2021.
- [23] T. Hu, Y. Huang, J. Chen, Q. Wu, and Z. Gong, "3D radio map reconstruction based on generative adversarial networks under constrained aircraft trajectories," *IEEE Trans. Veh. Technol.*, vol. 72, no. 6, pp. 8250–8255, Jan. 2023.
- [24] S. Timilsina, S. Shrestha, and X. Fu, "Quantized radio map estimation using tensor and deep generative models," *IEEE Trans. Signal Process.*, vol. 72, pp. 173–189, Nov. 2024.
- [25] S. Shrestha, X. Fu, and M. Hong, "Deep spectrum cartography: Completing radio map tensors using learned neural models," *IEEE Trans. Signal Process.*, vol. 70, pp. 1170–1184, Jan. 2022.
- [26] X. Wang, K. Tao, N. Cheng, Z. Yin, Z. Li, Y. Zhang, and X. Shen, "RadioDiff: An effective generative diffusion model for sampling-free dynamic radio map construction," *IEEE Trans. Cogn. Commun. Netw.*, vol. 11, no. 2, pp. 738–750, Apr. 2025.
- [27] X. Luo, Z. Li, Z. Peng, M. Chen, and Y. Liu, "Denoising diffusion probabilistic model for radio map estimation in generative wireless networks," *IEEE Trans. Cognitive Commun. Networking*, vol. 11, no. 2, pp. 751–763, Jan. 2025.
- [28] Y. Gong, H. Zhao, K. Hu, Q. Lu, and Y. Shen, "A multipath-aided localization method for MIMO-OFDM systems via tensor decomposition," *IEEE Wirel. Commun. Lett.*, vol. 11, no. 6, pp. 1225–1228, Jun. 2022.
- [29] A. Sayeed, "Deconstructing multiantenna fading channels," *IEEE Trans. Signal Process.*, vol. 50, no. 10, pp. 2563–2579, Oct. 2002.
- [30] J. Du, J. Cao, L. Jin, S. Li, J. Liu, and F. Gao, "Indoor vehicle positioning for MIMO-OFDM WIFI systems via rearranged sparse Bayesian learning," *IEEE Trans. Wireless Commun.*, vol. 23, no. 7, pp. 7849–7864, Jul. 2024.
- [31] D. P. Bertsekas, "Nonlinear programming," *Journal of the Operational Research Society*, vol. 48, no. 3, pp. 334–334, 1997.
- [32] F. A. Potra and S. J. Wright, "Interior-point methods," *J. Comput. Appl. Math.*, vol. 124, no. 1-2, pp. 281–302, Dec. 2000.
- [33] J. A. Bazerque, G. Mateos, and G. B. Giannakis, "Group-lasso on splines for spectrum cartography," *IEEE Trans. Signal Process.*, vol. 59, no. 10, pp. 4648–4663, Oct. 2011.
- [34] J. Liu, P. Musialski, P. Wonka, and J. Ye, "Tensor completion for estimating missing values in visual data," *IEEE Trans. Pattern Anal. Mach. Intell.*, vol. 35, no. 1, pp. 208–220, Jan. 2013.